crystals

MDPI

Article

Enhancement of Thermoelectric Performance of Donor-Doped ZnO Ceramics by Involving an In Situ Aluminothermic Reaction during Processing

Gabriel Constantinescu [1,*], Andrei Galatanu [2], David Tobaldi [3], Sergey Mikhalev [4], Diana Suarez [1], Tiago Paulino [1], Kiryl Zakharchuk [1], Sergii Sergiienko [1], Daniela Lopes [1] and Andrei Kovalevsky [1,*]

[1] Department of Materials and Ceramic Engineering, CICECO—Aveiro Institute of Materials, University of Aveiro, 3810-193 Aveiro, Portugal
[2] Laboratory of Magnetism and Superconductivity, National Institute of Materials Physics, 077125 Magurele, Romania
[3] CNR-NANOTEC—Institute of Nanotechnology, 73100 Lecce, Italy
[4] Department of Mechanical Engineering, TEMA—Centre for Mechanical Technology and Automation, University of Aveiro, 3810-193 Aveiro, Portugal
* Correspondence: gabriel.constantinescu@ua.pt (G.C.); akavaleuski@ua.pt (A.K.)

Abstract: This work explores the possibility of involving aluminothermy in processing donor-doped zinc oxide-based thermoelectrics by relying on local, strong exothermic effects developed during sintering, with a potential positive impact on the electrical and thermal transport properties. The strategy was exemplified by using aluminium as a dopant, due to its recognized ability to generate additional, available charge carriers in ZnO, and by using two different metallic Al powders and conventional Al_2O_3 as precursors. Nanosized aluminium powder was involved in order to evaluate the possible desirable effects of the particles size, as compared to aluminium micropowder. A significant enhancement of the electrical and thermoelectric performance of the samples prepared via metallic Al precursors was observed and discussed in terms of the potential impacts provided by the aluminothermic reaction on the microstructure, charge carrier concentration and mobility during sintering. Although the presented results are the first to show evidence of how aluminothermic reactions can be used for boosting the thermoelectric performance of zinc oxide materials, the detailed mechanisms behind the observed enhancements are yet to be understood.

Keywords: Al-doped ZnO; aluminothermy; ceramics processing; transport properties; thermoelectric performance

Citation: Constantinescu, G.; Galatanu, A.; Tobaldi, D.; Mikhalev, S.; Suarez, D.; Paulino, T.; Zakharchuk, K.; Sergiienko, S.; Lopes, D.; Kovalevsky, A. Enhancement of Thermoelectric Performance of Donor-Doped ZnO Ceramics by Involving an In Situ Aluminothermic Reaction during Processing. *Crystals* **2022**, *12*, 1562. https://doi.org/10.3390/cryst12111562

Academic Editor: Konstanze R. Hahn

Received: 29 September 2022
Accepted: 29 October 2022
Published: 2 November 2022

1. Introduction

Around half of today's energy is still generated using one type or another of fossil fuel. Furthermore, ~50% of that initial energy is lost to the environment as wasted heat. This very poor energy management and all its correlated effects, together with the increasing world population, have led to critical problems over time, most of them related to sustainability and global warming. Thermoelectric (TE) power generation stands out as a promising solution capable of successfully tackling most of those problems in a very effective manner. This technology can safely use waste heat sources (such as from conventional combustion engine exhaust, for example) to produce electricity directly, thanks to the Seebeck effect [1]. This "green" TE technology can only be used at a larger scale and compete with current, in-use, sources of energy if the performance and efficiency (typically at around 5%) of the corresponding TE materials and TE generators are further improved [2,3]. Nevertheless, TE technology is autonomous, reliable, scalable, robust, has no moving parts, and requires virtually no maintenance, making it ideal for mobile and/or remote applications [4].

The performance of a TE material is always limited by the Carnot efficiency [5] and is measured by the dimensionless figure-of-merit $ZT = (\alpha^2\sigma)/\lambda T$, where α is the absolute

Seebeck coefficient, σ is the electrical conductivity, λ is the total thermal conductivity, and T is the prospective working temperature [2]. The electrical part of ZT ($\alpha^2\sigma$) represents the power factor (PF) and depends entirely on the material's intrinsic physical properties.

Established TE materials have ZT around unity and include PbTe, Bi_2Te_3, Bi_2Se_3, filled skutterudite, half-Heusler alloys, intermetallic Zintl phases, and some Si-based alloys. Most of them are narrow band-gap semiconductors and have optimum performances at low and intermediate working temperature ranges. Because of some limitations/drawbacks (degradation and decomposition at temperatures above ~400–500 °C, thermal and/or chemical instability, expensive, toxic, and/or scarce constituents), they are not suitable for waste heat recovery applications above those temperatures [6].

Among the different candidates for high-temperature power generation applications, donor-doped ZnO stands out as a promising solution, due to its obvious advantages, such as low price and high abundance, as well as its promising electrical, catalytic, photochemical, and optoelectronic properties [7]. Different state-of-the-art n-doped ZnO ceramics usually exhibit attractive electrical properties together with relatively high thermal conductivities above room temperature [8,9]. Nanograin engineering and different nanocomposite concepts have been found to be promising approaches in decreasing the thermal conductivity of this material [10,11]. It has been found that the TE properties and performance of ZnO can be controlled by doping or co-doping with chemical species with oxidation states equal to 2+ or higher and with sizes comparable to that of Zn from the wurtzite structure, such as Ni [12], Fe [13], Bi [14], and, most importantly, Al [15,16].

Al-doped ZnO ceramics are focused for high temperature TE applications due to the relatively high charge carrier mobility values stemming from the covalent bonding and the small difference in electronegativity between zinc and oxygen [17].

This work focused on a different processing approach for the preparation of improved zinc oxide-based TEs. The small metallic aluminium additions from this work are simultaneously used as dopants and sintering additives, promoting the strong in situ exothermic reactions capable of improving the densification during sintering and the production of additional charge carriers.

From the displacement reaction between Al and ZnO [18]:

$$2Al + 3ZnO \rightarrow Al_2O_3 + 3Zn + \Delta H, \quad (1)$$

where the enthalpy $\Delta H(T)$ is given by [19]:

$$\Delta H(T) = \Delta H(0) + \int \Delta C_p dT, \quad (2)$$

it can be clearly seen that there is a net production of excess heat (the in situ aluminothermic reactions) and metallic zinc, available for aluminothermy.

The dopant diffusion and the defect chemistry are strongly affected by the processing conditions and the presence of steep temperature gradients in the studied materials. The exothermic effects provided by the aluminothermic reaction [20] are expected to be potentially interesting in this sense. The wurtzite structure of zinc oxide offers very limited solubility for almost all appropriate donor dopant cations ([21] and references therein), including traditional aluminium [17,22], even at high temperatures. A $ZnAl_2O_4$ spinel by-product can also form under such conditions, decreasing the actual doping level [11,15,16,23]. Using extremely high temperatures for sintering donor-doped ZnO is not feasible, both from an economical viewpoint and taking into account the zinc oxide evaporation ([24] and references therein). The creation of local overheating conditions might promote the dopant dissolution and other favourable micro-/nanostructural effects, while maintaining the integrity of the ceramics, especially when a low dopant content is used in ZnO, as in our case. These arguments served as a motivation for the present work.

2. Materials and Methods

Ceramic powders/samples with the nominal composition $Zn_{0.995}Al_{0.005}O$ were prepared from reagent grade precursors, namely ZnO powder (99.99%, metal basis, Alfa Aesar, CAS number: 1314-13-2) and 3 different sources of Al: nanometric Al powder (99.995%, 770 nm metal basis, Nanografi, CAS number: 7429-90-5), micrometric Al powder (325 mesh, 99.5%, metal basis, APS 7-15 microns, Alfa Aesar, CAS number: 7429-90-5), and Al_2O_3 powder (10 microns, 99.7% trace metals basis, Sigma-Aldrich, CAS number: 1344-28-1).

The 3 different types of Al-doped ZnO compositions (batches of 20 g) were prepared by simply mixing and grinding the 2 components (10 min) in an agate mortar with pestle, followed by an ultrasonification step in an ultrasound bath (10 min), both under absolute ethanol medium. After the ethanol was evaporated in a drying oven, the homogeneous powders were uniaxially pressed (around 15 kN or 220 MPa) into pellets (10 mm and 15 mm diameter) and bars (15 mm × 5 mm × 3 mm), which were then subsequently sintered in air at 1300 °C for 10 h, with 5 °C/min heating and cooling ramps.

After sintering, the resulted samples were polished, finely ground or cut in the adequate shapes and sizes, for the relevant characterizations to be performed onward.

The experimental densities (ρ_{exp}) of the various $Zn_{0.995}Al_{0.005}O$ ceramics were determined by the geometrical measurements and weighing (masses over volumes) of several samples of the same sort. The estimated errors in all cases were found to be <3% (~0.03 g/cm^3). The calculated ρ_{exp} values were then compared to the theoretical density (ρ_{th}) value of pristine polycrystalline ZnO precursor (5.67 g/cm^3, from PDF Card #04-003-2106).

The phase identification in the different $Zn_{0.995}Al_{0.005}O$ samples was performed using powder X-ray Diffraction (XRD) analyses, at room temperature, using a Panalytical X'Pert PRO3 system (Malvern Panalytical) working with CuK_α radiation (Cu_α = 1.54060 Å), with 2θ angles ranging from 5 to 90°, and a step and exposure time of 0.02° 2θ and 3 s, respectively. The phase content was estimated using the reference intensity ratio (RIR) method [25], using the Panalytical HighScore Plus 4.1 (PDF-4) software (Malvern Panalytical). The strongest peaks from each phase were used for analysis, and the corresponding scale factors were taken from the PDF-4 database.

The apparent optical bandgap energy (E_g) was calculated from the diffuse reflectance spectroscopy (DRS) data collected from finely ground sintered ceramic samples, between 250–825 nm (UV-VIS range), every 0.2 nm, using a UV-3100 UV-VIS-NIR Spectrophotometer (Shimadzu) equipped with an integrating sphere, and a white SPECTRALON certified reflectance standard reference (Labsphere, SRS-99-010, AS-01160-060, S/N 99AA03-1115-3432) for a 100% (full) reflectance calibration. A more detailed description of the involved procedures can be found elsewhere [26].

The morphological and microstructural characterizations of representative fractures from selected samples (coated with carbon) were performed with a SU-70 scanning electron microscope (SEM) instrument (Hitachi), equipped with an Quantax 400 energy-dispersive X-ray spectroscopy (EDX) detector module (Bruker).

Simultaneous electrical conductivity (σ) and Seebeck coefficient (α) measurements were performed on selected rectangular bar-shaped samples (~10 mm × 2 mm × 2 mm) in constant air flow, from 1175 K to 475 K, with a step of 50 K and followed by up to 0.5 h of thermal equilibration at each temperature, employing a steady-state technique and using a custom, "home-made" experimental setup described in detail elsewhere [27]. Freshly cut samples of each composition were fixed inside a specially designed alumina sample holder and placed inside a high-temperature furnace, one horizontally (σ sample, electrically connected with fine Pt wires, following a four-point probe direct current, DC technique arrangement) and the other vertically (α sample, subjected to a local constant temperature difference of ~14 K). The estimated experimental error in measured values did not exceed 3–5% for the conductivity and 5–7% for Seebeck coefficient. The power factor values were calculated from the measured σ and α values, in each case, at each temperature step.

The thermal transport properties were investigated using a LFA 457 MicroFlash system (Netzsch), between room temperature and 1175 K, with a step of 50 K in the transversal mode, on disk shaped samples with thicknesses of 1.00 mm. The measurement was performed in Ar (99.999% purity) and air fluxes. The equipment allows for the direct measurement of thermal diffusivity, while the specific heat capacity Cp is determined by a differential method, using a reference sample (in this case Al_2O_3, NIST SRM-720). The total thermal conductivity λ is then calculated by $\lambda = \alpha \times \rho_{exp} \times Cp$, with ρ_{exp} being the experimental density and α the diffusivity of the sample, in this case. The dimensionless figure of merit was calculated from the measured thermal conductivity values and the calculated power factor values, in each case, at each temperature step.

The various plots were constructed using the OriginPro 8.5 software (OriginLab). The hexagonal wurtzite unit cell image was constructed with the VESTA (Visualization for Electronic and STructural Analysis) software (Ver 3.5.7., 64-bit edition, JP-Minerals).

The lattice parameters, unit-cell volumes, and agreement factors (fitting parameters) were calculated from the raw diffraction patterns data in each case, using the profile matching method from the WinPLOTR [28] program (version: April 2014) of the FULLPROF software (2.05, version: July 2011, ILL).

3. Results and Discussion

From this point onwards, the different $Zn_{0.995}Al_{0.005}O$ ceramic samples made from Al_2O_3, micrometric Al and nanometric Al powders will be denoted as ZAOO, microZAO, and nanoZAO, respectively. The main reference samples are the ones prepared from alumina powder, namely ZAOO.

An example of typical $Zn_{0.995}Al_{0.005}O$ samples prepared in this work can be seen in Figure 1 below. These bars and disks present a light blue-green hue, indicative of the Al doping, as well as a minimum 10% shrinkage in size, with respect to the initial dimensions (before sintering). Such bars and disks were further processed (polished, cut, grinded) and prepared for the different analyses subsequently performed.

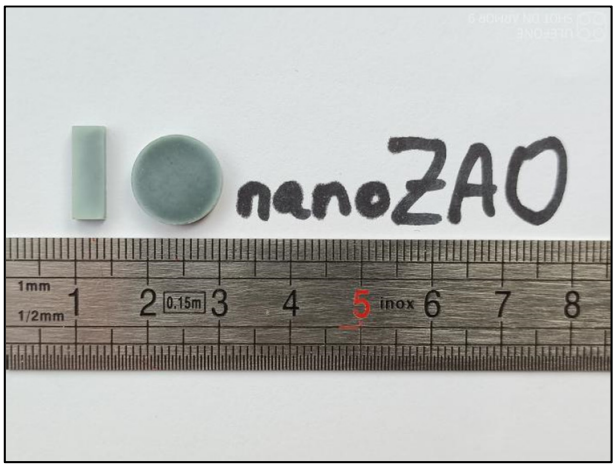

Figure 1. A set of typical $Zn_{0.995}Al_{0.005}O$ samples (nanoZAO composition) prepared via aluminothermic reactions and used in the different analyses performed in this work.

The room-temperature powder XRD patterns of the prepared materials are shown in Figure 2. All reflections can be indexed as corresponding to a hexagonal wurtzite structure (ICDD reference pattern #04-009-7657), with a negligible difference between the samples. This is expected since the dopant content is very low and, in many cases, the concentration of possible impurities, such as $ZnAl_2O_4$ spinel and unreacted aluminium oxide, is below the detection limit of standard XRD equipment [21].

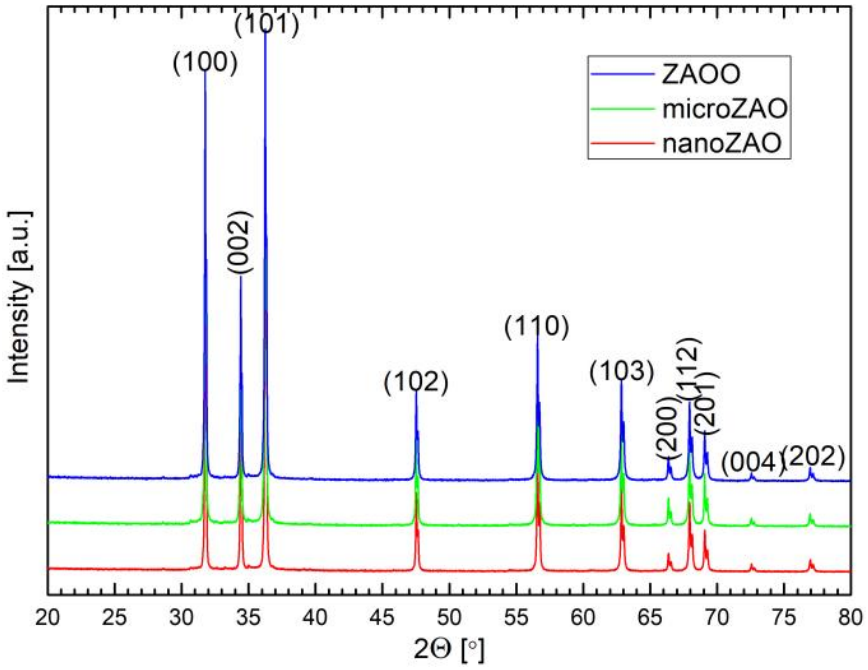

Figure 2. Powder XRD patterns and reflection planes for the three different $Zn_{0.995}Al_{0.005}O$ samples.

The observed similarity of the structural parameters appears self-evident, since the samples have the same nominal chemical composition. However, this does not imply that the actual donor doping level is the same for all samples. Various controversies were previously reported regarding the effect of the aluminium content on the lattice parameters of the ZnO wurtzite phase [29,30]. In fact, aluminium incorporation may occur through the substitutional and/or interstitial mechanisms with opposite effects on the unit cell volume [29]. A major effect on the TE performance is expected when the substitutional mechanism predominates, resulting in n-type charge carrier generation.

A typical unit cell representation of this direct bandgap semiconductor [31] can be seen in Figure 3a, while a Fullprof fitting example for the ZAOO reference sample (including the crystallographic planes) can be observed in Figure 3b. The peak fitting parameters used for the Rietveld refinement in all cases were the following: background, atomic parameters (Z, B, Occ), and profile parameters (Factors, Cell Parameters, FWHM/Shape Parameters). The wurtzite structure representative for ZnO consists of two interpenetrating hexagonal close packed (hcp) sublattices of Zn and O cations and anions, respectively, displaced by the length of a cation–anion bond in the c-direction. Each sublattice includes four atoms per unit cell, and every atom of one type (group II atom) is surrounded by four atoms of the other type (group VI) or vice versa, which are coordinated at the edges of a tetrahedron. In an ideal wurtzite structure, the c/a ratio is 1.633 [7]. From the column 3 of Table 1, it is obvious that the c/a ratio of our real ZnO based samples is slightly smaller than that of the ideal structure, most probably due to the different imperfections found in the actual crystal lattice.

Using the XRD and Rietveld refinement data, the mean crystallite sizes (D) were calculated for all 3 compositions (first 3 peaks), via the Williamson–Hall (W-H) and Scherrer (S) methods, and the results can be seen in the Table 2 below. The average crystallite sizes present a steep decrease from the ZAOO to the microZAO samples, followed by a light increase in the case of nanoZAO. These trends are believed to be a consequence of the morphology of the different sources of Al used and will be better explained and understood in the following section concerning microstructural discussions.

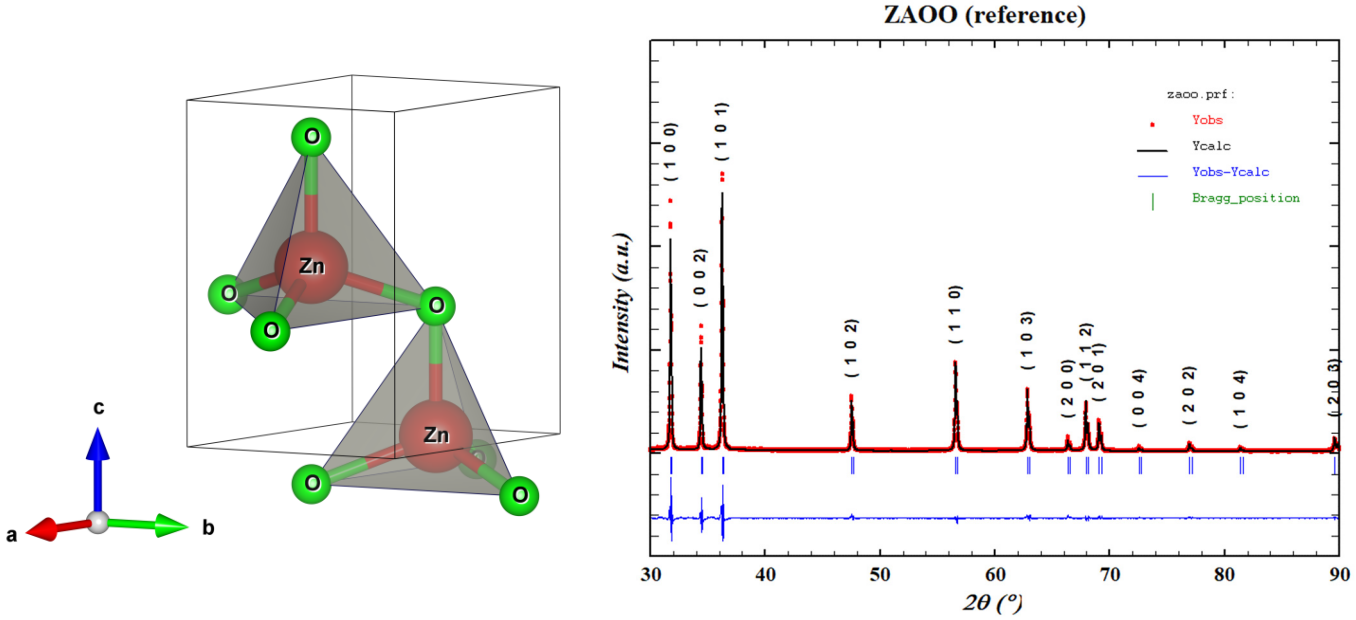

Figure 3. A hexagonal wurtzite unit cell simplified view (**a**) and a Fullprof fitting example for the ZAOO reference sample, including the crystallographic planes (**b**).

Table 1. Lattice parameters, unit cell volumes, agreement factors, experimental density and apparent optical band-gap energy values for the three different $Zn_{0.995}Al_{0.005}O$ samples.

Sample	$a = b$, nm	c, nm	c/a	$V_{uc}x10^3$, nm^3	R_p	R_{wp}	ρ_{exp}, g/cm^3	ρ_{exp}/ρ_{th}, %	E_g, eV
ZAOO (reference)	0.3250(2)	0.5207(0)	1.6020(4)	47.63(6)	6.59	8.51	5.23(1)	92	3.15(1)
microZAO	0.3250(5)	0.5208(2)	1.6022(6)	47.65(7)	7.13	9.24	5.44(3)	96	3.16(1)
nanoZAO	0.3250(3)	0.5206(8)	1.6019(4)	47.63(8)	7.66	9.70	5.46(2)	96	3.16(1)

Table 2. Average crystallite sizes (D) calculated for the three different $Zn_{0.995}Al_{0.005}O$ samples via the Williamson–Hall (W-H) and Scherrer (S) methods.

Sample	D (W-H), nm	D (S), nm
ZAOO (reference)	97.9(4)	100.6(0)
microZAO	87.6(1)	91.7(3)
nanoZAO	95.2(2)	98.6(0)

The representative microstructures of the sintered ceramic samples are shown in Figure 4. Dense ceramics were obtained, with the relative density increasing from the sample prepared using Al_2O_3 powder precursor to the samples processed from metallic aluminium precursors (Table 1). The microstructural images (Figure 4), however, suggest the presence of residual porosity, with the pores space filled with Al-rich particles, presumably Al_2O_3, in all cases. The level of these particles appears larger in the case of ZAOO (with larger pores), than for the microZAO and nanoZAO samples (with smaller pores), and their morphology is also different when comparing the samples prepared using Al_2O_3 and metallic Al in terms of the morphologies of the 3 Al-source precursors, as seen in Figure 5. Such inhomogeneities most likely stem from the non-uniform mixing of the components even after the ultrasonic treatments, as well as from the different reaction rates taking place during sintering. Secondly, all the precursor powders, including Al nanopowder, show a notable agglomeration (Figure 5). It can be seen that, in this case, to demonstrate the possible contribution of the aluminothermic reaction, the samples were sintered in one step without intermediate calcinations and were usually involved in other works to improve the

homogenization during solid state processing (e.g., [8,16,26,30,32]). In fact, soft chemistry methods followed by fast sintering are preferable for the preparation of high-performing zinc oxide-based TEs [23,33–36], because they usually allow more uniform dopant distribution and nanostructuring to decrease the intrinsically high thermal conductivity of ZnO-based materials. However, adjusting such routes for preparing uniform mixtures containing nanostructured zinc oxide and metallic aluminium nanoparticles is challenging.

While in the case of Al_2O_3 precursor (ZAOO sample) the remaining Al_2O_3 particles are integrated into the pore walls (Figure 4f), the remaining Al rich particles appear detached and fill in the pore volume, as in the case of the microZAO sample (Figure 4d), or are simply sintered together, in the case of nanoZAO (Figure 4a). These differences in morphology may originate from the local overheating effects taking place during the aluminothermic reaction of aluminium with zinc oxide (see Equation (1)), considering the different morphologies of the Al precursors seen in Figure 5.

The standard enthalpy of the reaction from Equation (1), ΔH^0_{298}, is -625 kJ/mol [20]. The onset temperature of the reaction depends on the size of aluminium particles and can also be tuned by the mechanical activation of the powder mixture [18].

As an example, the DSC studies suggest that the exothermic effect corresponding to aluminothermy can be observed in a wide temperature range of 910–1280 K, depending on the powder morphology and heating rate [18,20], which, in most cases, is above the melting point of aluminium (933 K). Metallic aluminium particles are usually covered with a thin oxide film which prevents their further oxidation even on heating in air. For the latter, the kinetics of oxidation depends on the heating rate. On heating, the difference in thermal expansion of metallic aluminium and oxide will produce mechanical stresses and cracks, especially during the melting of aluminium [18]. Once the integrity of the oxide film is destroyed, metallic aluminium will come in contact with zinc oxide, resulting in the onset of the aluminothermic reaction.

It is important to notice that, considering the sintering condition used in the present work, one can expect that the intensive direct oxidation of metallic aluminium in air will only occur at temperatures above 1273 K [37–39]. Thus, the aluminothermic reaction is expected to prevail during the heating process, producing local hot spots and affecting the microstructure and transport properties of the samples.

Figure 6 shows the variations of electrical properties (sigma and alpha) with temperature. All doped samples demonstrate a weak temperature dependence on the electrical conductivity at high temperatures, typical for degenerate semiconductors. This tendency becomes more pronounced for the samples prepared using the metallic precursors and, especially, for the nanoZAO sample. In the same figure, the results for pure, undoped ZnO samples are also added in order to highlight their typical low and high electrical conductivity and Seebeck coefficient values, respectively, and thus to showcase the superior properties of our novel, Al-doped samples in a wider frame of reference.

The measured values of the electrical conductivity of the doped samples are in the range of those typically observed in the literature for air-sintered samples [8,21,33,36,40,41]. However, at lower temperatures, the electrical conductivity shows more irregular behaviour and transition from nearly metallic to thermally activated behaviour, which can be discussed in terms of the changes in scattering mechanisms and grain boundaries effects [42,43]. The negative sign of the Seebeck coefficient confirms the n-type conduction in the prepared materials.

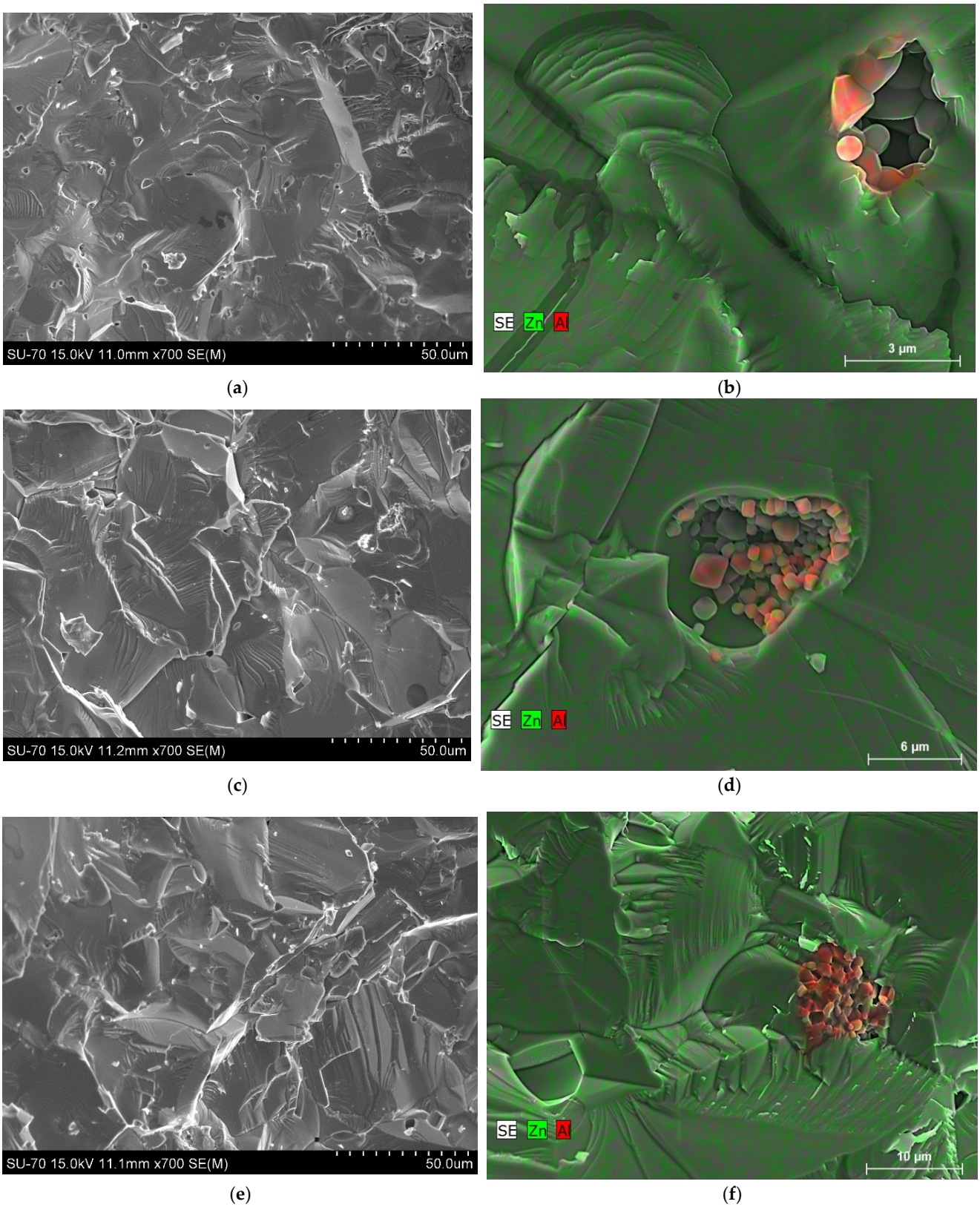

Figure 4. Representative SEM micrographs (**a**,**c**,**e**) and EDS maps (**b**,**d**,**f**) of the transversal fractures of nanoZAO (**a**,**b**), microZAO (**c**,**d**), and the reference ZAOO (**e**,**f**) samples.

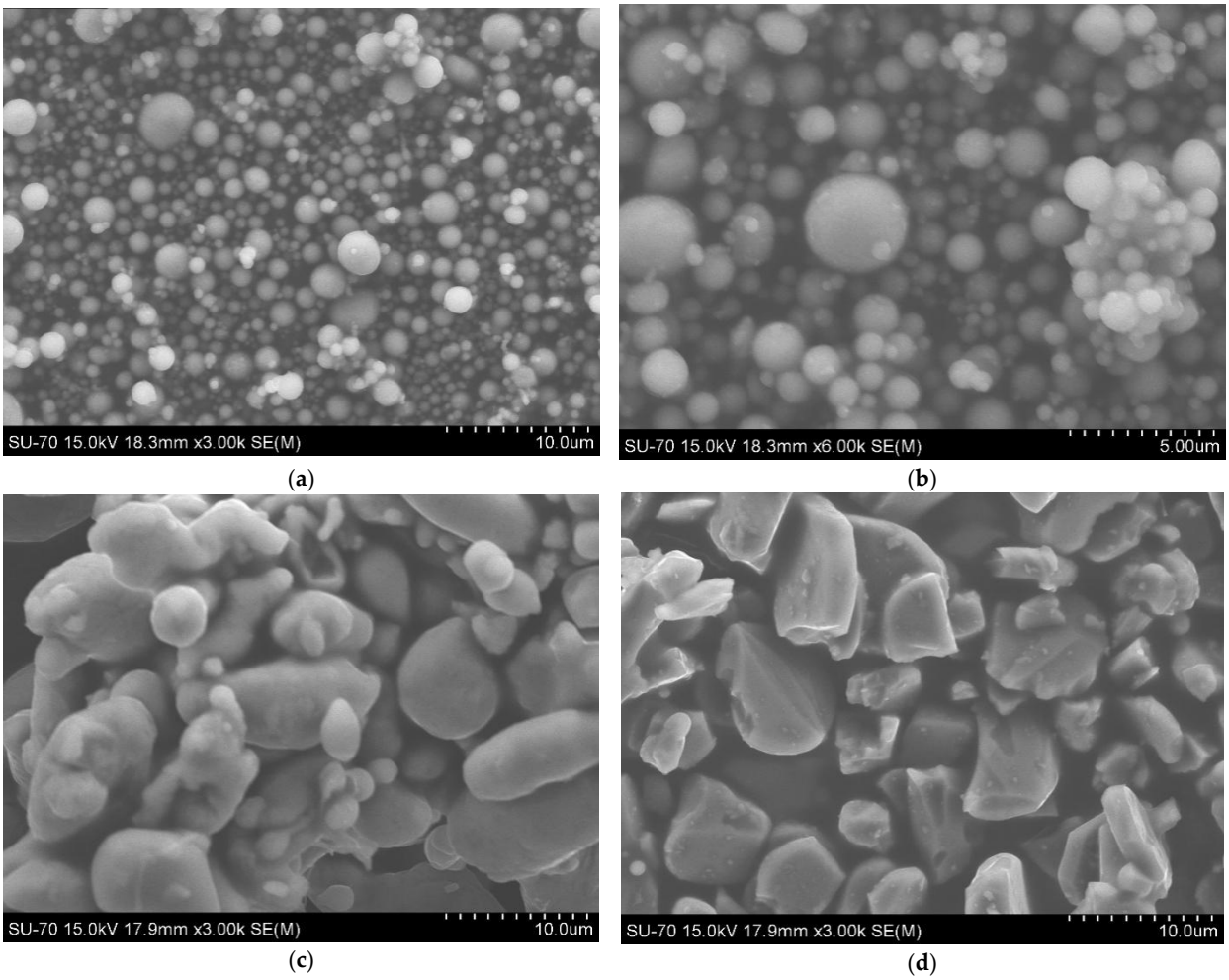

Figure 5. Representative SEM micrographs of the precursor's powders: nanometric Al powder (**a**,**b**), micrometric Al powder (**c**), and Al_2O_3 (**d**).

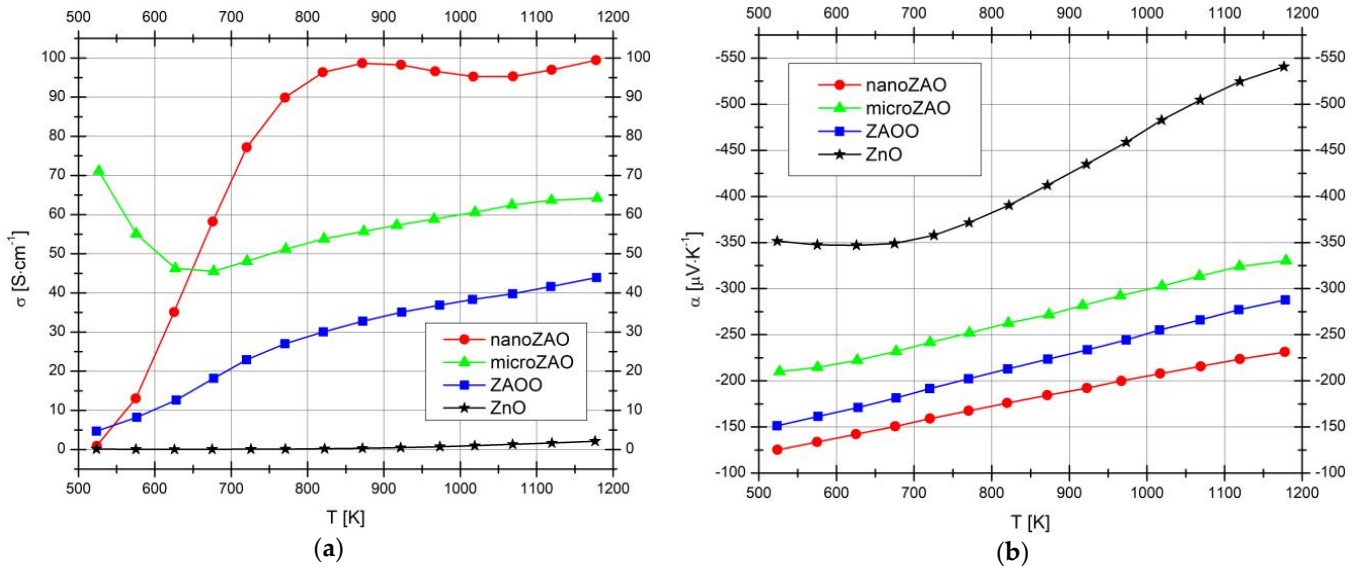

Figure 6. Temperature-dependence of the electrical conductivity (**a**) and Seebeck coefficient (**b**) for the three different $Zn_{0.995}Al_{0.005}O$ samples. The results for pure, undoped ZnO samples are also added, for a more general comparison.

Both samples prepared using metallic Al precursor show notably higher electrical conductivity compared to the conventionally prepared ZAOO sample. At 800–850 K, more than a 3-fold increase in conductivity is observed for the nanoZAO sample. This improvement appears counterintuitive when analysing these results together with the microstructural data. The images from Figure 4a,d, which represent a general picture found for these samples, suggest that a significant part of the aluminium precursor may actually remain unreacted, decreasing the actual doping level. The density improvement from 92 to 96% in the samples prepared via aluminothermic reaction is not sufficient to explain such a significant boost of the electrical conductivity. A plausible explanation is that local and strongly exothermic aluminothermic reactions promote the incorporation of aluminium into the wurtzite structure by the substitutional mechanism, resulting in the generation of additional charge carriers. At the same time, while using the conventional process for the ZAOO sample, part of the aluminium can be incorporated as interstitials and/or the formation of $ZnAl_2O_4$ spinel might occur [16]. Due to the low nominal aluminium concentration and the absence of additional components which promote the spinel formation [16], it was not possible to detect its presence in any amounts for the discussed samples.

It should be noticed that the proposed mechanism which relies on the increase in charge carrier concentration could be debatable, taking into account the measured values of the optical band gap (Table 1), which are essentially similar for all the samples. Still, these values were obtained at ambient temperatures, where, indeed, the electrical conductivity of the ZAOO and nanoZAO samples converge, while still demonstrating the high electrical conductivity of microZAO sample, could be attributed to the effects imposed by the measuring route from high to low temperatures. The low-temperature trapping of the charge carriers at the grain boundaries [44] and competing band gap widening due to the Burstein–Moss effect and its narrowing due to approaching the Mott critical density of the charge carriers [30,44] might also contribute to the resulting similar optical band gap energy found for the prepared materials.

Some additional guidelines on the relevant mechanisms behind the observed boosting of the electrical conductivity in the samples processed using metallic Al can be obtained from the Seebeck coefficient results (Figure 6b). The thermopower decreases for nanoZAO sample as compared to ZAOO, suggesting that, most probably, the observed conductivity enhancement is linked to an increase of the charge carrier concentration. However, the microZAO sample surprisingly shows the highest Seebeck coefficient (not considering the pure, undoped ZnO), and the reasons for that are still to be understood. It is very likely that aluminothermic-boosted sintering might also enhance the mobility of the charge carriers. More detailed studies of the microstructure by HRTEM and Hall effect measurements are required to prove or reject this hypothesis. In any case, the observed results show that a significant improvement in electrical contribution to the TE performance can be achieved if metallic aluminium precursor is used instead of conventional Al_2O_3. The latter is well-illustrated by the power factor values presented in Figure 7. A maximum enhancement of the power factor was achieved for the microZAO samples, due to a simultaneous increase in the electrical conductivity and Seebeck coefficient values.

The thermal conductivity data is presented in Figure 8. Minor variations of the thermal conductivity with the composition are expected, since the samples have similar and relatively low dopant contents, while their microstructures were also mostly similar. The electronic contribution to the thermal conductivity is below 5%, indicating that a major part of the heat is transferred by the phonons. Although the difference is almost within the experimental error, the lowest thermal conductivity at 500–750 K was observed for the nanoZAO sample, indicating that some additional phonon scattering contributions might actually be provided, due to the use of the nanometric-scale Al powder as a precursor.

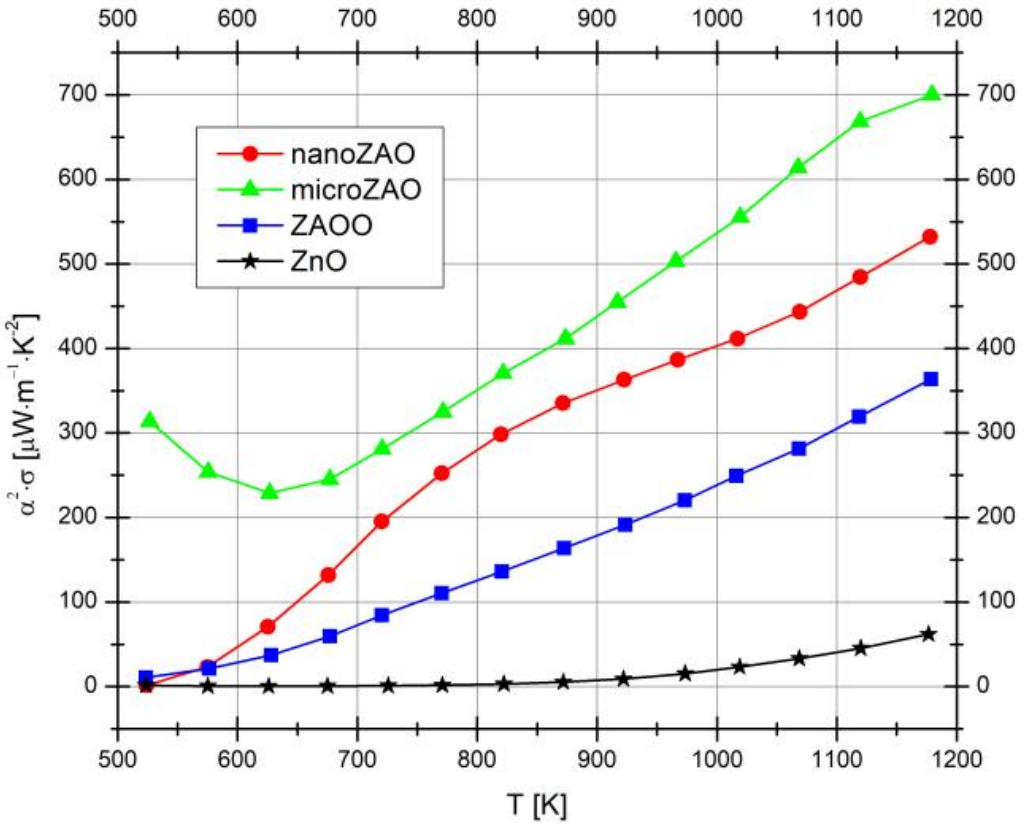

Figure 7. Temperature-dependence of the electrical power factor for the three different $Zn_{0.995}Al_{0.005}O$ samples. The results for pure, undoped ZnO samples are also added for a more general comparison.

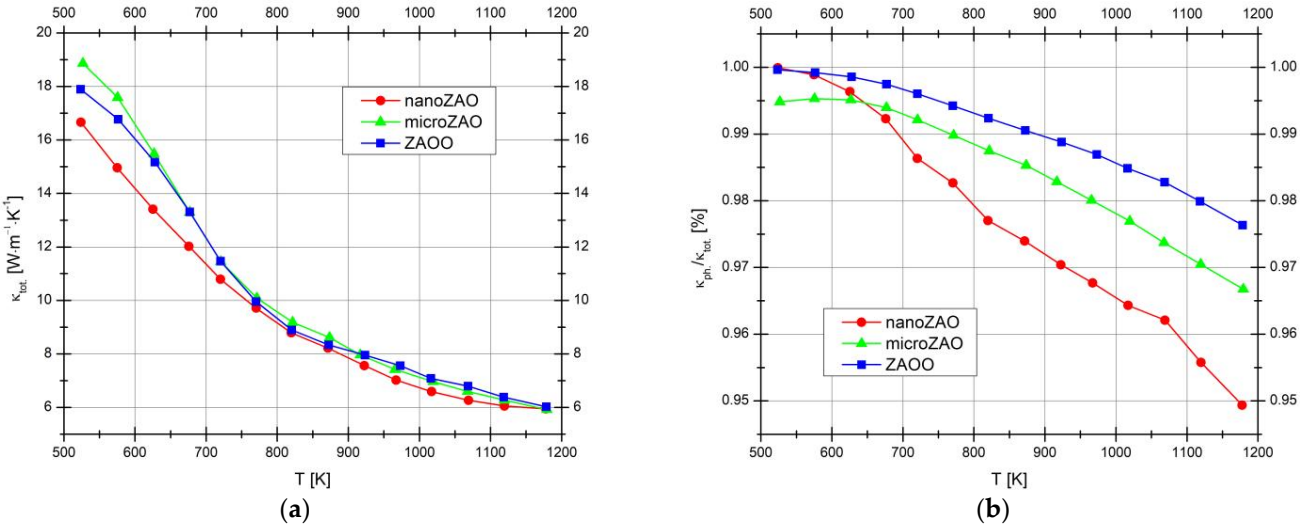

Figure 8. Temperature dependence of the total thermal conductivity (**a**) and phonon contribution to the total thermal conductivity (**b**) for the three different $Zn_{0.995}Al_{0.005}O$ samples.

Finally, the combined effect of the electrical and thermal transport properties on the overall TE performance is illustrated by the temperature-dependence of the dimensionless figure of merit shown in Figure 9. The most notable enhancement reaching ZT of 0.14 at 1173 K was observed for the microZAO sample. The overall improvement of the ZT in nanoZAO and microZAO samples is mainly linked to electrical performance. This first evidence of how aluminothermic reactions can be involved in the processing of TEs based

on zinc oxide, however, leaves several important questions unanswered regarding the relevant mechanisms behind the observed effects.

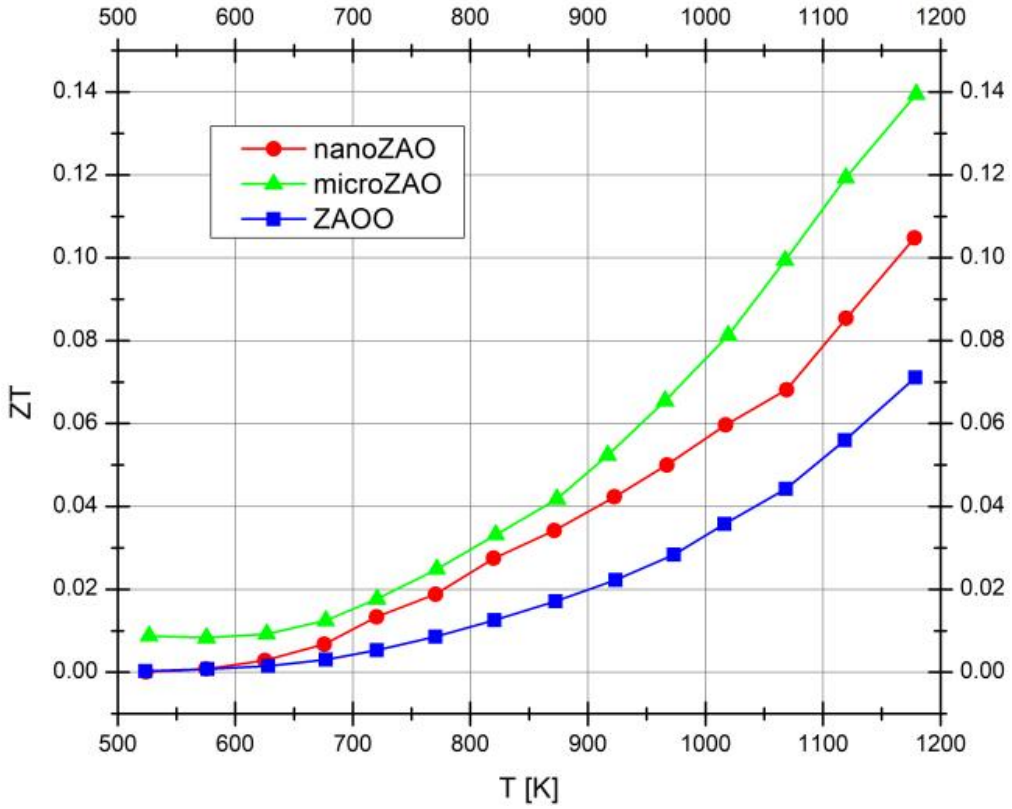

Figure 9. Temperature dependence of the dimensionless figure-of-merit for the three different $Zn_{0.995}Al_{0.005}O$ samples.

Significant room for the optimization of the applied sample preparation procedures also exists, including faster sintering rates and the better homogenization of the precursor mixtures. Eventually, the approach could be extended to the combination of the different metallic precursors, aiming for co-doped compositions based on ZnO.

4. Conclusions

Ceramic samples with the stoichiometry $Zn_{0.995}Al_{0.005}O$ were prepared using Al_2O_3 and metallic Al, involving the standard solid-state route under identical conditions. XRD, optical, and microstructural studies revealed only minor differences between the sintered samples, mainly related to the inhomogeneous distribution of aluminium. A significant 2-3-fold increase in electrical conductivity at temperatures above 850 K is observed for the samples prepared using metallic aluminium, being attributed to the effect of the aluminothermic reaction during sintering, affecting the charge carrier concentration and mobility. A high Seebeck coefficient corresponding to (−210)–(−330) μV/K at 523–1173 K was measured for ceramics prepared using metallic Al micropowder. The precursor type was found to have almost no effect on the thermal conductivity of the ceramic samples. The maximum power factor values and dimensionless figure of merit of 700 $\mu Wm^{-1}K^{-2}$ and 0.14 at 1173 K, respectively, were obtained for $Zn_{0.995}Al_{0.005}O$ ceramics, prepared using metallic aluminium micrometric powder and marking almost a two-time increase as compared to the sample processed using a conventional Al_2O_3 precursor.

Author Contributions: Conceptualization, G.C. and A.K.; Data curation, G.C.; Formal analysis, G.C., D.T. and A.K.; Funding acquisition, G.C. and A.K.; Investigation, G.C., A.G., S.M., D.S., T.P., K.Z., S.S. and D.L.; Methodology, G.C., A.G., D.T., S.M. and A.K.; Project administration, G.C. and A.K.; Resources, G.C. and A.K.; Software, S.M.; Supervision, G.C. and A.K.; Validation, S.M., D.S., T.P., K.Z.,

S.S. and D.L.; Visualization, G.C. and A.K.; Writing—original draft, G.C. and A.K.; Writing—review and editing, G.C., A.G., D.T., S.M., D.S., T.P., K.Z., S.S., D.L. and A.K. All authors have read and agreed to the published version of the manuscript.

Funding:  This project has received funding from the European Commission Union's Horizon 2020 research and innovation programme. 101003375. 

Institutional Review Board Statement: Not applicable.

Informed Consent Statement: Not applicable.

Data Availability Statement: Not applicable.

Acknowledgments: Gabriel Constantinescu acknowledges the support of the TEOsINTE project (Grant agreement ID: 101003375), funded under the H2020-EU.4.Programmes (Funding Scheme: MSCA-IF-EF-ST—Standard EF). This work was developed also within the scope of the project CICECO-Aveiro Institute of Materials, UIDB/50011/2020, UIDP/50011/2020 and LA/P/0006/2020, financed by national funds through the FCT/MEC (PIDDAC). David M. Tobaldi is grateful to the project EleGaNTe—PON ARS01_01007 (CUP: B91G18000200005). Diana Suarez is grateful for the participation in the CICECO Open Project for Young Scientists (CICECO Young Scientist Program) "A Unileg-type thermoelectric generator built from new ceramic composites".

Conflicts of Interest: The authors declare no conflict of interest. The funders had no role in the design of the study; in the collection, analyses, or interpretation of data; in the writing of the manuscript; or in the decision to publish the results.

References

1. Beretta, D.; Neophytou, N.; Hodges, J.M.; Kanatzidis, M.G.; Narducci, D.; Martin-Gonzalez, M.; Beekman, M.; Balke, B.; Cerretti, G.; Tremel, W.; et al. Thermoelectrics: From history, a window to the future. *Mater. Sci. Eng. R Rep.* **2019**, *138*, 100501. [CrossRef]
2. Freer, R.; Powell, A.V. *Realising the Potential of Thermoelectric Technology: A Roadmap*; Royal Society of Chemistry: London, UK, 2020; Volume 8, pp. 441–463.
3. Bahrami, A.; Schierning, G.; Nielsch, K. Waste Recycling in Thermoelectric Materials. *Adv. Energy Mater.* **2020**, *10*, 1904159. [CrossRef]
4. Champier, D. Thermoelectric generators: A review of applications. *Energy Convers. Manag.* **2017**, *140*, 167–181. [CrossRef]
5. Karana, D.R.; Sahoo, R.R. Influence of geometric parameter on the performance of a new asymmetrical and segmented thermoelectric generator. *Energy* **2019**, *179*, 90–99. [CrossRef]
6. LeBlanc, S. Thermoelectric generators: Linking material properties and systems engineering for waste heat recovery applications. *Sustain. Mater. Technol.* **2014**, *1*, 26–35. [CrossRef]
7. Morkoç, H.; Özgür, Ü. *Zinc Oxide: Fundamentals, Materials and Device Technology*; John Wiley & Sons: Hoboken, NJ, USA, 2009; ISBN 9783527408139.
8. Tian, T.; Cheng, L.; Zheng, L.; Xing, J.; Gu, H.; Bernik, S.; Zeng, H.; Ruan, W.; Zhao, K.; Li, G. Defect engineering for a markedly increased electrical conductivity and power factor in doped ZnO ceramic. *Acta Mater.* **2016**, *119*, 136–144. [CrossRef]
9. Giovannelli, F.; Chen, C.; Díaz-Chao, P.; Guilmeau, E.; Delorme, F. Thermal conductivity and stability of Al-doped ZnO nanostructured ceramics. *J. Eur. Ceram. Soc.* **2018**, *38*, 5015–5020. [CrossRef]
10. Han, L.; Van Nong, N.; Zhang, W.; Hung, L.T.; Holgate, T.; Tashiro, K.; Ohtaki, M.; Pryds, N.; Linderoth, S. Effects of morphology on the thermoelectric properties of Al-doped ZnO. *RSC Adv.* **2014**, *4*, 12353–12361. [CrossRef]
11. Jood, P.; Mehta, R.J.; Zhang, Y.; Peleckis, G.; Wang, X.; Siegel, R.W.; Borca-Tasciuc, T.; Dou, S.X.; Ramanath, G. Al-doped zinc oxide nanocomposites with enhanced thermoelectric properties. *Nano Lett.* **2011**, *11*, 4337–4342. [CrossRef]
12. Colder, H.; Guilmeau, E.; Harnois, C.; Marinel, S.; Retoux, R.; Savary, E. Preparation of Ni-doped ZnO ceramics for thermoelectric applications. *J. Eur. Ceram. Soc.* **2011**, *31*, 2957–2963. [CrossRef]
13. Liang, X. Thermoelectric transport properties of Fe-enriched ZNO with high-temperature nanostructure refinement. *ACS Appl. Mater. Interfaces* **2015**, *7*, 7927–7937. [CrossRef] [PubMed]

14. Jood, P.; Mehta, R.J.; Zhang, Y.; Borca-Tasciuc, T.; Dou, S.X.; Singh, D.J.; Ramanath, G. Heavy element doping for enhancing thermoelectric properties of nanostructured zinc oxide. *RSC Adv.* **2014**, *4*, 6363–6368. [CrossRef]
15. Ohtaki, M.; Tsubota, T.; Eguchi, K.; Arai, H. High-temperature thermoelectric properties of (Zn1-xAlx)O. *J. Appl. Phys.* **1996**, *79*, 1816–1818. [CrossRef]
16. Zakharchuk, K.V.; Widenmeyer, M.; Alikin, D.O.; Xie, W.; Populoh, S.; Mikhalev, S.M.; Tselev, A.; Frade, J.R.; Weidenkaff, A.; Kovalevsky, A.V. A self-forming nanocomposite concept for ZnO-based thermoelectrics. *J. Mater. Chem. A* **2018**, *6*, 13386–13396. [CrossRef]
17. Tsubota, T.; Ohtaki, M.; Eguchi, K.; Arai, H. Thermoelectric properties of Al-doped ZnO as a promising oxide material for high-temperature thermoelectric conversion. *J. Mater. Chem.* **1997**, *7*, 85–90. [CrossRef]
18. Maleki, A.; Panjepour, M.; Niroumand, B.; Meratian, M. Mechanism of zinc oxide-aluminum aluminothermic reaction. *J. Mater. Sci.* **2010**, *45*, 5574–5580. [CrossRef]
19. Chen, G.; Sun, G.X. Study on in situ reaction-processed Al-Zn/α-Al2O3(p) composites. *Mater. Sci. Eng. A* **1998**, *244*, 291–295. [CrossRef]
20. Maleki, A.; Hosseini, N.; Niroumand, B. A review on aluminothermic reaction of Al/ZnO system. *Ceram. Int.* **2018**, *44*, 10–23. [CrossRef]
21. Arias-Serrano, B.I.; Mikhalev, S.M.; Ferro, M.C.; Tobaldi, D.M.; Frade, J.R.; Kovalevsky, A.V. On the high-temperature degradation mechanism of ZnO-based thermoelectrics. *J. Eur. Ceram. Soc.* **2021**, *41*, 1730–1734. [CrossRef]
22. Shirouzu, K.; Ohkusa, T.; Hotta, M.; Enomoto, N.; Hojo, J. Distribution and solubility limit of AI in Al2O 3-doped ZnO sintered body. *J. Ceram. Soc. Jpn.* **2007**, *115*, 254–258. [CrossRef]
23. Gautam, D.; Engenhorst, M.; Schilling, C.; Schierning, G.; Schmechel, R.; Winterer, M. Thermoelectric properties of pulsed current sintered nanocrystalline Al-doped ZnO by chemical vapour synthesis. *J. Mater. Chem. A* **2015**, *3*, 189–197. [CrossRef]
24. Kim, J.S.; Kim, J.W.; Cheon, C.I.; Kim, Y.S.; Nahm, S.; Byun, J.D. Effect of chemical element doping and sintering atmosphere on the microwave dielectric properties of barium zinc tantalates. *J. Eur. Ceram. Soc.* **2001**, *21*, 2599–2604. [CrossRef]
25. Hubbard, C.R.; Snyder, R.L. RIR—Measurement and Use in Quantitative XRD. *Powder Diffr.* **1988**, *3*, 74–77. [CrossRef]
26. Arias-Serrano, B.I.; Xie, W.; Aguirre, M.H.; Tobaldi, D.M.; Sarabando, A.R.; Rasekh, S.; Mikhalev, S.M.; Frade, J.R.; Weidenkaff, A.; Kovalevsky, A.V. Exploring tantalum as a potential dopant to promote the thermoelectric performance of zinc oxide. *Materials* **2019**, *12*, 2057. [CrossRef]
27. Kovalevsky, A.V.; Yaremchenko, A.A.; Populoh, S.; Weidenkaff, A.; Frade, J.R. Enhancement of thermoelectric performance in strontium titanate by praseodymium substitution. *J. Appl. Phys.* **2013**, *113*, 053704. [CrossRef]
28. Roisnel, T.; Rodríguez-Carvajal, J. WinPLOTR: A windows tool for powder diffraction pattern analysis. In *Materials Science Forum*; Transtec Publications: Brüttisellen, Switzerland, 2001; Volume 378–381, pp. 118–123.
29. Nakrela, A.; Benramdane, N.; Bouzidi, A.; Kebbab, Z.; Medles, M.; Mathieu, C. Site location of Al-dopant in ZnO lattice by exploiting the structural and optical characterisation of ZnO: Al thin films. *Results Phys.* **2016**, *6*, 133–138. [CrossRef]
30. Zakharchuk, K.V.; Tobaldi, D.M.; Xiao, X.; Xie, W.; Mikhalev, S.M.; Martins, J.F.; Frade, J.R.; Weidenkaff, A.; Kovalevsky, A.V. Synergistic effects of zirconium- and aluminum co-doping on the thermoelectric performance of zinc oxide. *J. Eur. Ceram. Soc.* **2019**, *39*, 1222–1229. [CrossRef]
31. Ivanov, I.; Pollmann, J. Electronic structure of ideal and relaxed surfaces of ZnO: A prototype ionic wurtzite semiconductor and its surface properties. *Phys. Rev. B* **1981**, *24*, 7275–7296. [CrossRef]
32. Pashkevich, A.V.; Fedotov, A.K.; Poddenezhny, E.N.; Bliznyuk, L.A.; Fedotova, J.A.; Basov, N.A.; Kharchanka, A.A.; Zukowski, P.; Koltunowicz, T.N.; Korolik, O.V.; et al. Structure, electric and thermoelectric properties of binary ZnO-based ceramics doped with Fe and Co. *J. Alloys Compd.* **2022**, *895*, 162621. [CrossRef]
33. Sulaiman, S.; Sudin, I.; Al-Naib, U.M.B.; Omar, M.F. Review of the Nanostructuring and Doping Strategies for High-Performance ZnO Thermoelectric Materials. *Crystals* **2022**, *12*, 1076. [CrossRef]
34. Zhang, D.B.; Li, H.Z.; Zhang, B.P.; Liang, D.D.; Xia, M. Hybrid-structured ZnO thermoelectric materials with high carrier mobility and reduced thermal conductivity. *RSC Adv.* **2017**, *7*, 10855–10864. [CrossRef]
35. Kim, K.H.; Shim, S.H.; Shim, K.B.; Niihara, K.; Hojo, J. Microstructural and thermoelectric characteristics of zinc oxide-based thermoelectric materials fabricated using a spark plasma sintering process. *J. Am. Ceram. Soc.* **2005**, *88*, 628–632. [CrossRef]
36. Zhou, B.; Chen, L.; Li, C.; Qi, N.; Chen, Z.; Su, X.; Tang, X.F. Significant Enhancement in the Thermoelectric Performance of Aluminum-Doped ZnO Tuned by Pore Structure. *ACS Appl. Mater. Interfaces* **2020**, *12*, 51669–51678. [CrossRef] [PubMed]
37. Hasani, S.; Panjepour, M.; Shamanian, M. Non-isothermal kinetic analysis of oxidation of pure aluminum powder particles. *Oxid. Met.* **2014**, *81*, 299–313. [CrossRef]
38. Velasco, F.; Guzmán, S.; Moral, C.; Bautista, A. Oxidation of micro-sized aluminium particles: Hollow alumina spheres. *Oxid. Met.* **2013**, *80*, 403–422. [CrossRef]
39. Hasani, S.; Panjepour, M.; Shamanian, M. The oxidation mechanism of pure aluminum powder particles. *Oxid. Met.* **2012**, *78*, 179–195. [CrossRef]
40. Guilmeau, E.; Maignan, A.; Martin, C. Thermoelectric oxides: Effect of doping in delafossites and zinc oxide. *J. Electron. Mater.* **2009**, *38*, 1104–1108. [CrossRef]
41. Vogel-Schäuble, N.; Dujardin, R.; Weidenkaff, A.; Aguirre, M.H. Influence of thermal aging phenomena on thermoelectric properties of al-substituted ZnO. *J. Electron. Mater.* **2012**, *41*, 1606–1614. [CrossRef]

42. Han, L.; Christensen, D.V.; Bhowmik, A.; Simonsen, S.B.; Hung, L.T.; Abdellahi, E.; Chen, Y.Z.; Nong, N.V.; Linderoth, S.; Pryds, N. Scandium-doped zinc cadmium oxide as a new stable n-type oxide thermoelectric material. *J. Mater. Chem. A* **2016**, *4*, 12221–12231. [CrossRef]
43. Kinemuchi, Y.; Mikami, M.; Kobayashi, K.; Watari, K.; Hotta, Y. Thermoelectric properties of nanograined ZnO. *J. Electron. Mater.* **2010**, *39*, 2059–2063. [CrossRef]
44. Roth, A.P.; Webb, J.B.; Williams, D.F. Absorption edge shift in ZnO thin films at high carrier densities. *Solid State Commun.* **1981**, *39*, 1269–1271. [CrossRef]